GE

Form Approved
OBM No. 0704-0188

1. Agency Use Only, 1994

3. Report Type and Dates Covered.
Final - Journal Article

4. Title and Subtitle.
Broadband Source Imaging in a Shallow Water Wedge by an Array of Receivers

5. Funding Numbers.
Program Element No. 601153N
Project No. 03202
Task No. 350
Accession No. DN255005
Work Unit No. 12242B

6. Author(s).
Feuillade, C. and Clay, C.*

7. Performing Organization Name(s) and Address(es).
Naval Research Laboratory
Ocean Acoustics Branch
Stennis Space Center, MS 39529-5004

8. Performing Organization Report Number.
Journal of Acoustical Society of America, Vol. 96, No. 1, July 1994, pp. 501-514

9. Sponsoring/Monitoring Agency Name(s) and Address(es).
Naval Research Laboratory
Center for Environmental Acoustics
Stennis Space Center, MS 39529-5004

10. Sponsoring/Monitoring Agency Report Number.
NRL/JA/7174--92-0002

11. Supplementary Notes.
*University of Wisconsin-Madison
Madison, WI 53706

12a. Distribution/Availability Statement.
Approved for public release; distribution is unlimited.

12b. Distribution Code.

13. Abstract *(Maximum 200 words).*

The combination of time domain source imaging techniques and arrays to consider the localization of an impulsive source in a wedge waveguide, with a free surface and rigid bottom, is investigated. An impulsive signal is transmitted from an unknown location, received by an array of hydrophones, and stored. The signals are time reversed and transmitted into the model wedge by a transducer at each receiver location. Model transmission functions are used to compute the pressures at a set of locations. The field calculations use an image construction from D. Chu's exact solution for a density contrast wedge [J. Acoust. Soc. Am. 86, 1883-1896 (1989)]. A map of the peak pressures gives an image of the source location. Particular attention is given to the peak amplitudes, sidelobe amplitudes, and spatial resolution as a function of the number and placement of receivers. Source localization is enhanced by the range dependency of the environment, which eliminates "range" sidelobes, even for a single hydrophone. Adding receivers along an arc eliminates "angle" sidelobes; but adding receivers along an arc or radial gives little reduction in overall background level. Adding receivers parallel to the wedge axis gives sharp, unambiguous azimuthal imaging.

14. Subject Terms.
Shallow-water; algorithms; hydrophone arrays; source imaging techniques

15. Number of Pages.
14

16. Price Code.

17. Security Classification of Report.	18. Security Classification of This Page.	19. Security Classification of Abstract.	20. Limitation of Abstract.
Unclassified	Unclassified	Unclassified	SAR

DISCLAIMER NOTICE

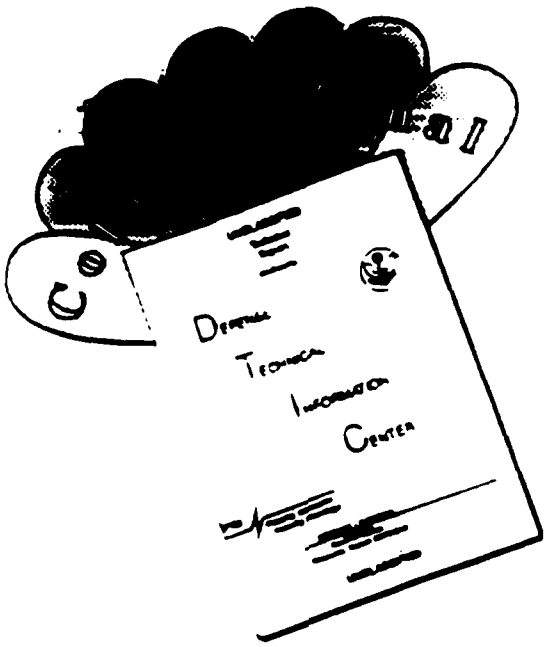

THIS DOCUMENT IS BEST QUALITY AVAILABLE. THE COPY FURNISHED TO DTIC CONTAINED A SIGNIFICANT NUMBER OF COLOR PAGES WHICH DO NOT REPRODUCE LEGIBLY ON BLACK AND WHITE MICROFICHE.

Broadband source imaging in a shallow water wedge by an array of receivers

Christopher Feuillade
Naval Research Laboratory, Stennis Space Center, Mississippi 39529-5004

Clarence S. Clay
Geophysical and Polar Research Center, University of Wisconsin-Madison, 1215 W. Dayton Street, Madison, Wisconsin 53706

(Received 2 June 1993; accepted for publication 31 January 1994)

The combination of time domain source imaging techniques and arrays to consider the localization of an impulsive source in a wedge waveguide, with a free surface and rigid bottom, is investigated. An impulsive signal is transmitted from an unknown location, received by an array of hydrophones, and stored. The signals are time reversed and transmitted into the model wedge by a transducer at each receiver location. Model transmission functions are used to compute the pressures at a set of locations. The field calculations use an image construction from D. Chu's exact solution for a density contrast wedge [J. Acoust. Soc. Am. **86**, 1883–1896 (1989)]. A map of the peak pressures gives an image of the source location. Particular attention is given to the peak amplitudes, sidelobe amplitudes, and spatial resolution as a function of the number and placement of receivers. Source localization is enhanced by the range dependency of the environment, which eliminates "range" sidelobes, even for a single hydrophone. Adding receivers along an arc eliminates "angle" sidelobes; but adding receivers along an arc or radial gives little reduction in overall background level. Adding receivers parallel to the wedge axis gives sharp, unambiguous azimuthal imaging.

PACS numbers: 43.20.Mv, 43.30.Vh, 43.30.Wi, 43.35.Sx

INTRODUCTION

There are two extreme types of sources: Sources of continuous wave harmonic pressures and sources of broad frequency bandwidth pressures. Source location methods differ for the two kinds of sources. Matched field techniques for harmonic sources require an array of receivers.[1–4] Matched signal methods use wide frequency bandwidth signals and as few as a single receiver.[5–10] Both methods use many observations of the field in the waveguide but do it differently. Matched field methods typically use the observations at an array of receivers and a single frequency. Matched signal methods may use observations at many frequencies and one receiver. Both methods give ambiguity or image maps and these maps can have large "false" images or peaks that rival or dominate the proper image at the source location.

Since matched signal methods can use a single receiver to get a source location, does an array of receivers "improve" the image or ambiguity maps? There are many ways to measure any improvement that may be obtained. Here we choose to use the ratio of the maximum of the false (or "sidelobe") peaks to the peak at the matched position or source location. The spatial resolution of the image is also of interest. Numerical studies of source location in a Pekeris waveguide have shown that the false peaks were reduced by increasing the number of receivers in an array; however, the results were not dramatic.[10] Matched-mode methods and time domain methods can be combined.[11]

As an extension of our previous research in a waveguide having parallel boundaries,[10] we study the wedge waveguide. To emphasize the role of the receiver array in the image mapping process and simplify the numerical work, we use an ideal wedge waveguide.[12] The exact solutions for the wedge do not require intensive numerical computations. For the same reason, we use a pulse transmission instead of a random source with the same signal bandwidth.

The acoustical source location method used here is, using an optical analogy, a holographic imaging technique. The array of receivers samples and records the outward traveling wave field of the source. If recorded signals are transmitted by an array of transducers at the receiver locations, then the wave field continues traveling outward as if it came from the source. If the recorded signals are time reversed and then transmitted by the array of transducers, the backward traveling wave fields converge to form an image of the source at the source location. The time reversal technique is also known as phase conjugation because the complex conjugate of the spectral function gives a time reversal of the signal.[12,14] Imaging techniques are highly developed in exploration seismology where they are known as "migration", "imaging," and "impulse holography".[13,15] Ideally, the back projected wave fields are shown as a moving picture as the waves travel in the waveguide. Instead of showing a motion picture or a sequence of snapshots, we make a quasistatic image of the image field by displaying the maximum absolute values of the wave fields at a closely spaced grid of points.

Exact solutions for wave fields in a wedge are in Biot and Tolstoy[16] and Chu.[17] While this theory provides a basis for doing the required calculations exactly, the computations are fast and easily programmed. The method facilitates the investigation of source imaging in the wedge as a function of bandwidth (by varying the time duration of the transmitted pulse) and the number and placement of receivers (by performing reciprocal calculations to multiple receivers at different locations in the wedge and aggregating the results). While we use the formulation of Biot and Tolstoy and Chu in

 0001-4966/94/96(1)/501/14/$6.00

this paper because it is simple and direct, Buckingham[18] has given a different formulation for calculating the sound field in a wedge due to continuous wave sources. His method included reflection beyond the critical angle, [illegible]e beam displacement technique described by Brekh[illegible][19] and used in several applications.[20–23]

Section I of this paper gives a brief review of useful expressions from wedge theory, image construction rays, and the time reversed transmission technique. Section II discusses the imaging of acoustic fields. Section III describes the environmental model and signal transmissions. Section IV describes measures of localization. Section V discusses single receiver and pulse duration effects. Section VI discusses array designs. This is followed by a summary of the conclusions drawn from the study. We have included an appendix which describes the geometrical-kaleidoscopic method for constructing reflected ray paths. This shows how ray path calculations may be performed in wedges with arbitrary reflection coefficients at the boundaries and also in finite wedges.

I. THEORY: ACOUSTIC FIELDS IN A WEDGE

The time domain impulsive solution for the wedge problem has tremendous advantages compared to the single frequency harmonic normal mode solution. The Biot–Tolstoy time domain expressions are a sophisticated solution of the wave equation.[12,16,17,24] In the time domain, all of the reflection arrivals and the diffraction from the wedge apex are identifiable and separated. Depending on the practical situation, we can keep, modify, and discard any of the arrivals.

The theory for the wedge was given as an example of normal coordinate applications to problems in wave propagation [Biot and Tolstoy (1957)].[16] The normal coordinate method comes from analytic mechanics and is often called the Lagrangian method. Readers are referred to Chap. 3 and Appendix 5 of Tolstoy and Clay, *Ocean Acoustics* (1987),[12] and Chap. 8 of Tolstoy, *Wave Propagation* (1973)[24] for normal coordinate methods in wave propagation. The original Biot and Tolstoy solution was for an impulsive point source in a wedge that has rigid boundaries. Later, Kinney *et al.*[25] gave a solution for the wedge with free boundaries. Chu derived the exact impulse response of a density contrast wedge.[17] He also derived expressions for a half-space of air over a half-space that contains a density contrast wedge.[26] This paper also contains an extensive list of references on the wedge problem. For the reader's convenience we give here a synopsis of solutions for the different boundary conditions. In the shallow water waveguide and similar problems the diffraction arrival from the wedge apex is likely to be unimportant relative to the contributions from the image part of the solution.

The coordinates and geometry are shown in Fig. 1. The wedge apex is along the y axis. The boundary planes of the wedge are normal to the x-z plane. The angles are measured counter clockwise from the lower wedge face. These choices let us use the z coordinate for depth and to have the x and y coordinates in the horizontal plane. The source is in the x-z plane at $y=0$. The receiver can be displaced a distance y. The radial distance from the y axis is r. The wedge angle Θ_w

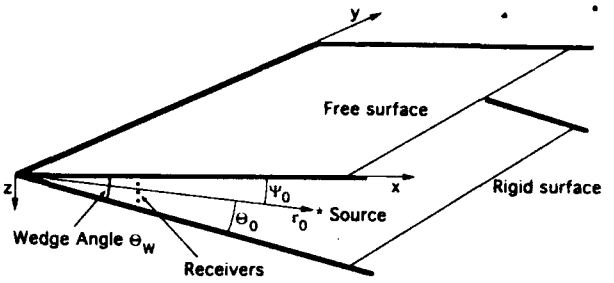

FIG. 1. Geometry and coordinates for wedge. In this figure the coordinates of the source are labeled $(r_0,0,\Psi_0)$ and those of the receiver (r,y,Ψ), where the angles Ψ_0, Ψ are measured down from the top (free) surface of the wedge. The wedge angle is Θ_w. The angles Θ_0, Θ (for the source and receiver, respectively) used in Sec. I are measured up from the bottom (rigid) surface of the wedge. They are $\Theta_0=\Theta_w-\Psi_0$ and $\Theta=\Theta_w-\Psi$.

can have any value, $0<\Theta_w\leq 2\pi$. The sound velocity is c. Biot and Tolstoy[12,16] and Tolstoy[24] use the displacement potential ϕ and solve for $\partial\phi/\partial t$ for a unit step of displacement at the origin. Medwin replaced the step function in the volume source by a source that starts a constant flow S at $t=0$.[27] Then, the pressure response $p(t)$ is

$$p(t)=\{[P_0\ R_0]\delta(t-R/c)\}/R \tag{1}$$

for pressure P_0 at range R_0. We write these as $[P_0\ R_0]$ because they represent the source pressure and always go together to keep the dimensions correct. The change from $\partial\phi/\partial t$ to pressure from an impulsive pressure source uses

$$p(t)=-4\pi[P_0\ R_0]\frac{\partial\varphi}{\partial t}. \tag{2}$$

The derivation of the complete solution of the wedge problem is long. To facilitate the reader's reference to the Biot–Tolstoy and Tolstoy developments we use $\partial\phi/\partial t$ and then convert to $p(t)$ later. The changes from Biot–Tolstoy to the notations in Tolstoy, Chu, and here, are $\alpha\rightarrow c$, $\beta\rightarrow\gamma$, $z\rightarrow y$, $\zeta\rightarrow\Theta_w$, and $x\rightarrow\xi$. Three regions of the solution are defined by the values of t relative to t_0 and τ_0

$$t_0=(1/c)[(r-r_0)^2+y^2]^{1/2}, \tag{3}$$

$$\tau_0=(1/c)[(r+r_0)^2+y^2]^{1/2}. \tag{4}$$

We define the fields in each "time" region as

$$\frac{\partial\phi}{\partial t}=\frac{\partial\phi_1}{\partial t}+\frac{\partial\phi_2}{\partial t}+\frac{\partial\phi_3}{\partial t}, \tag{5}$$

where the regions occur in the time intervals $t<t_0$, $t_0\leq t<\tau_0$, and $\tau_0<t$.

A. Region 1: Before the first arrival and $t<t_0$

Region 1 needs little discussion because $\partial\phi_1/\partial t$ is zero prior to the arrival of a disturbance from the source. This is equivalent to requiring that the solution be causal

$$\frac{\partial\phi_1}{\partial t}=0,\quad t<t_0. \tag{6}$$

B. Region 2: Direct arrival and images and $t_0\leq t<\tau_0$

Here the solution is the sum of a finite number of images. The expression for fields in a wedge having rigid boundaries follows:

$$p(t)=-4\pi[P_0\ R_0]\frac{\partial\phi_2}{\partial t}$$

$$=[P_0\ R_0]\left(\sum_k \frac{\delta\{t-[R_k(+-)/c]\}}{R_k(+-)}\right.$$

$$+\sum_k \frac{\delta\{t-[R_k(-+)/c]\}}{R_k(-+)}+\sum_k \frac{\delta\{t-[R_k(++)/c]\}}{R_k(++)}$$

$$\left.+\sum_k \frac{\delta\{t-[R_k(--)/c]\}}{R_k(--)}\right), \tag{7}$$

where ct becomes $R_k(+-)$ etc. and these are given by

$$R_k(+-)=[r_0^2+r^2+y^2-2r_0r\cos(2k\Theta_w+\Theta-\Theta_0)]^{1/2},$$

$$R_k(-+)=[r_0^2+r^2+y^2-2r_0r\cos(2k\Theta_w-\Theta+\Theta_0)]^{1/2},$$

$$R_k(++)=[r_0^2+r^2+y^2-2r_0r\cos(2k\Theta_w+\Theta+\Theta_0)]^{1/2},$$

$$R_k(--)=[r_0^2+r^2+y^2-2r_0r\cos(2k\Theta_w-\Theta-\Theta_0)]^{1/2}.$$

The maximum value of k or $k_{\max}$ is given by the condition

$$0\leq|2k\Theta_w\pm\Theta\pm\Theta_0|\leq\pi. \tag{8}$$

This condition gives a finite number of images.

If one lets $k=-k_{\max},\ldots0,\ldots k_{\max}$, then $(2k\Theta_w+\Theta_0-\Theta)$ and $(2k\Theta_w-\Theta_0-\Theta)$ give all of the combinations. The pressure disturbance from the last image arrives before τ_0, the diffraction from the wedge apex. We show an image construction on Fig. 2. The images are reflections of the source in wedge planes. Possible image locations are on the circle containing the source and at the angles given by $2k\Theta_w\pm\Theta_0$ and $\Theta=0$. The choice of a receiver angle Θ requires that (8) be tested to determine the active images.

The rigid, free, and free-rigid boundaries can be written as follows

$$p(t)=-4\pi[P_0\ R_0]\frac{\partial\phi_2}{\partial t}$$

$$=[P_0\ R_0]\left(\sum_{k=-k_{\max}}^{k_{\max}} \mathcal{R}_{1,2}^{|k|}\mathcal{R}_{1,0}^{|k|}\frac{\delta\{t-[R_k(-+)/c]\}}{R_k(-+)}\right.$$

$$\left.+\sum_{k=-k_{\max}}^{k_{\max}} \mathcal{R}_{1,2}^{|k-1|}\mathcal{R}_{1,0}^{|k|}\frac{\delta\{t-[R_k(--)/c]\}}{R_k(--)}\right), \tag{9}$$

where $\mathcal{R}_{1,2}$ and $\mathcal{R}_{1,0}$ are the reflection coefficients at the interfaces. The direct arrival is given by $k=0$ and the $R_k(-+)$ term. When the source and receiver are near to each other or at the same place, one can drop this term. As Chu has shown,[17,26] $\mathcal{R}_{1,2}$ and $\mathcal{R}_{1,0}$ are not restricted to values of ±1, but can have any values between -1 and 1 for the isovelocity-density contrast wedge. The image arrivals are shown in Fig. 3.

C. Region 3: Diffraction and $t>\tau_0$

The final closed form expressions for the diffraction arrivals are the result of much manipulation. The expressions use the following parameters:

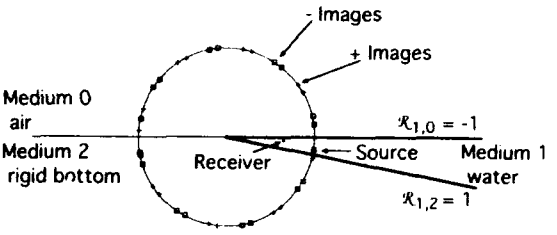

FIG. 2. Image construction for a free-rigid shallow water wedge waveguide. Wedge angle=11 deg. Source: angle 8 deg from surface and 3000 m range, $y=0$. Receiver: 4 deg from surface and 1000 m range, $y=0$.

$$\eta=\text{arc cosh}\ U,\quad \eta=\ln[U+(U^2-1)^{1/2}],$$
$$U\equiv[c^2t^2-(r^2+r_0^2+y^2)]/2r_0r\ ,\quad \nu=\pi/\Theta_W. \tag{10}$$

Rigid wedge boundaries (Biot–Tolstoy and Tolstoy)[12,16,24]

$$p(t)=-4\pi[P_0\ R_0]\frac{\partial\phi_3}{\partial t}$$
$$=\frac{-[P_0\ R_0]c}{2\Theta_W r r_0}[D(\eta,+-)+D(\eta,-+)$$
$$+D(\eta,++)+D(\eta,--)], \tag{11}$$

where

$$D(\eta,+-)\equiv\frac{\sin\nu(\pi+\Theta-\Theta_0)}{\sinh\eta\{\cosh[\nu(\eta+\delta)]-\cos\nu(\pi+\Theta-\Theta_0)\}} \tag{12}$$

and δ is a small damping number, typically 10^{-5} or a small fraction of a time step.

Free wedge boundaries (Kinney *et al.*)[25]

$$p(t)=-4\pi[P_0\ R_0]\frac{\partial\phi_3}{\partial t}$$
$$=\frac{-[P_0\ R_0]c}{2\Theta_W r r_0}[D(\eta,+-)+D(\eta,-+)$$
$$-D(\eta,++)-D(\eta,--)]. \tag{13}$$

Free-rigid wedge boundaries (Chu)[26]

$$p(t)=-4\pi[P_0\ R_0]\frac{\partial\phi_3}{\partial t}$$
$$=\frac{-[P_0\ R_0]c}{rr_0\Theta_w}[D_{r/f}(\eta,+-)+D_{r/f}(\eta,-+)$$
$$+D_{r/f}(\eta,++)+D_{r/f}(\eta,--)]. \tag{14}$$

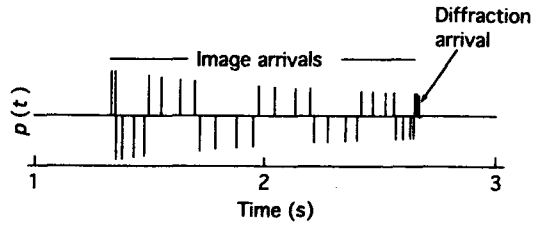

FIG. 3. Signal in an ideal shallow water wedge waveguide. Signal pressure $p(t)$ relative to the amplitude of the direct arrival. Source: angle 8 deg from surface and 3000 m range, $y=0$. Receiver: 4 deg from surface and 1000 m range, $y=0$. The input signal is a 2-ms spike.

$$D_{r/f}(\eta,+-)$$

$$\equiv\frac{\sin(\nu/2)(\pi+\Theta-\Theta_0)\cosh[(\nu/2)\eta+\delta/2]}{\sinh\ \eta\{\cosh[\nu(\eta+\delta)]-\cos\ \nu(\pi+\Theta-\Theta_0)\}}. \quad (15)$$

A sign and small algebraic error in Chu Eq. (14) are corrected.[26] For special values of Θ_w, the diffraction component is zero, i.e.,

$$\text{if } \Theta_W=\frac{\pi}{m} \text{ then } \frac{\partial\phi_3}{\partial t}=0, \quad (16)$$

where m is an integer. The images are the complete solution.

D. Numerical evaluations for very small η

These expressions (12)–(16) are easy to evaluate for $\eta>0$ or η greater than the first time step beyond τ_0 in a numerical evaluation. As t goes to τ_0, $\eta\to 0$, and $\partial\phi_3/\partial t$ becomes infinite. One can average $D(\Delta,+-)$ over the small time T_b or the first time step for robust evaluations.

$$D(\Delta,+-)|_{t\sim\tau_0}\approx\frac{1}{T_b}\int_0^{T_b}D(\Delta,+-)d\Delta, \quad \Delta\equiv t-\tau_0, \quad (17)$$

where $\Delta\ll\tau_0$. Numerical methods are in references.[10,17,26,28] Since those papers were written we have become ruthless in dropping small terms, because only the first time step is needed. Simplified results follow.

$$D(\Delta,+-)|_{t\sim\tau_0}\approx\frac{2\ \sin\ \nu(\pi+\Theta-\Theta_0)}{b\sqrt{T_b}[1-\cos\ \nu(\pi+\Theta-\Theta_0)+\delta^2/2]},$$

$$\eta\approx b\sqrt{\Delta}, \quad b\equiv c\sqrt{2\tau_0/rr_0}. \quad (18)$$

Similar operations on the free-rigid wedge (15) give

$$D_{r/f}(\eta,+-)|_{t\sim\tau_0}$$

$$\approx\frac{2\ \sin[\nu(\pi+\Theta-\Theta_0)/2]}{b\sqrt{T_b}[1-\cos\ \nu(\pi+\Theta-\Theta_0)+\delta^2/2]}. \quad (19)$$

An example of numerical evaluation for the free-rigid wedge is shown in Fig. 3. The diffraction arrival is the last event in Fig. 3. Comparisons of image amplitudes and the diffraction amplitude shows that the diffraction carries less than 0.1% of the energy.

Taking a practical view and assuming that the actual wedge apex is a lossy beach, the wedge apex is expected to be "leaky." Accordingly, the diffracted pressure component is expected to be negligible compared to the image contributions.[28] We ignore the diffraction arrival and keep the images.

II. IMAGING OF ACOUSTIC FIELDS

In our imaging discussion we identify the transmission in the real (actual) wedge as having the subscript A and the model wedge as having the subscript M. Presumably the model wedge is an accurate model of the actual wedge. We use our theoretical solutions to compute the transmission from a source any place in the model wedge to a probe receiver at position Q.

Briefly, the source at an unknown location transmits an impulsive signal and the transmission is received by a hydrophone and stored. The signal is time reversed. The time reversed signal is transmitted into the model wedge by a transducer at the receiver location. Model transmission functions are used to compute the pressures at a set of locations. A map of the peak pressures gives an image of the source location.

Recalling (9) and (11), the model transmission functions can be defined as follows:

$$f_M(t,H,Q)\equiv\left(\sum_{k=-k_{\max}}^{k_{\max}}\mathscr{R}_{1,2}^{|k|}\mathscr{R}_{1,0}^{|k|}\frac{\delta\{t-[R_k(-+)/c]\}}{R_k(-+)}\right.$$

$$\left.+\sum_{k=-k_{\max}}^{k_{\max}}\mathscr{R}_{1,2}^{|k-1|}\mathscr{R}_{1,0}^{|k|}\frac{\delta\{t-[R_k(--)/c]\}}{R_k(--)}\right) \quad (20)$$

and

$$f_M(t,H,Q)\equiv\frac{-c}{2\Theta_W r_Q r_H}[D(\eta,+-)+D(\eta,-+)$$

$$+D(\eta,++)+D(\eta,--)], \quad (21)$$

where the subscript H refers to the hydrophone at the receiver location (r_H, y_H, Θ_H) and Q the probe location (r_Q, y_Q, Θ_Q) and also S is the actual source location (r_S, y_S, Θ_S). Note that $f_M(t,H,Q)$ is a model transmission function and does not include the source function.

In the actual wedge, the pressure signal at the receiver for a transmission of $s(t)$ is the convolution

$$p_S(t)=s(t)*f_A(t,S,H), \quad (22)$$

where * indicates the convolution operation and we let $s(t)$ be the impulsive function $[P_0\ R_0]\delta(t)$. The time reverse is

$$p_S(-t)=s(-t)*f_A(-t,S,H)$$

$$=[P_0\ R_0]\delta(-t)*f_A(-t,S,H). \quad (23)$$

Using $\delta(t)=\delta(-t)$, the transmission of the time reversed signal into the model wedge gives the pressure at the probe position Q,

$$p_M(t,Q)=[P_0\ R_0]\delta(t)*f_A(-t,S,H)*f_M(t,H,Q). \quad (24)$$

The image is formed by mapping the peak of $|p_M(t,Q)|$ in the wedge as a function of (r_Q, y_Q, Θ_Q). At the matched position

$$c_A(t,S)=[P_0\ R_0]\delta(t)*f_A(-t,S,H)*f_A(t,H,S). \quad (25)$$

The operation $f_A(-t,S,H)*f_A(t,H,S)$ gives the covariance of the transmission function. We call this the correlation maximum.

Figure 4(a) shows an example of the pressure $p_M(t,S)$ at the matched location and Fig. 4(b) an example of the pressure $p_M(t,Q)$ at an unmatched location. In these figures, and in the rest of the paper, the source and receiver angles Ψ_S and Ψ_H etc. are measured clockwise from the top face of the wedge so that

$$\Psi_S = \Theta_W - \Theta_S,$$

$$\Psi_H = \Theta_W - \Theta_H,$$

and (26)

$$\Psi_Q = \Theta_W - \Theta_Q.$$

The lateral separation y is measured between the r-Θ plane that contains the source and the r-Θ plane that contains the receiver. An experimental verification of the time reverse transmission technique has been reported in the well known paper by Parvulescu and Clay.[29]

III. ENVIRONMENTAL MODEL AND TRANSMISSIONS

The environmental model used for this study is the three-dimensional wedge shown schematically in Fig. 1. We have a shallow isospeed water layer ($c=1500$ m/s) retained within the wedge, which has a free (pressure release) boundary at the water surface and a rigid bottom. The wedge angle is 11 deg. The positions of the source and receivers within the waveguide are shown schematically in the figure. A cylindrical coordinate system is used to specify their locations. The variables are the range r from the wedge apex; the horizontal distance y along the wedge axis; and the angle of declination Ψ from the water surface boundary. The source is placed so that $r_S=3000$ m, $y_S=0$ m, and Ψ_S lies between 0 and 11 deg. The receivers are placed such that typically $r_H \approx 1000$ m, y_H takes values between ± 250 m, and Ψ_H lies between 0 and 11 deg. One of the features of this study is the use of several receivers (displaced from each other by varying r_H, y_H, or Ψ_H) to study the effect on localization performance of multiple receiver channels. If only one receiver is used to filter the signal transmitted by the source, the hydrophone is positioned at $r_H=1000$ m, $y_H=0$ m, and $\Psi_H=4$ deg.

No acoustic attenuation is incorporated into the propagation paths (except $1/r$ spreading) or into the reflections at the wedge boundaries. Since the upper wedge boundary is a pressure release surface ($\mathscr{R}_{1,0}=-1$), a π phase change is introduced into the path each time a reflection at this boundary occurs. This causes the amplitude of the signal to change sign. In Fig. 3 we show the transmission from an impulsive source to a single receiver. The input signal is a 2-ms boxcar approximation to a delta function (a spike). The source is placed at $r_S=3000$ m, $y_S=0$ m, $\Psi_S=8$ deg. The first two arrivals are seen to have positive amplitude. These are due to signals transmitted directly from the source and from the first "+" image of the source reflected in the bottom surface of the wedge where $\mathscr{R}_{1,2}=1$ (see Fig. 2). The next four arrivals have negative amplitude. These come from the first four "−" images shown in Fig. 2. All of the ray paths here involve one reflection in the upper surface of the wedge and therefore undergo a π phase change. There are then another four arrivals with positive amplitude (from the next four "+" images). These ray paths undergo two reflections in the upper surface and so have two π phase changes (i.e., a total of 2π). The sequence of arrivals continues until all of the images shown in Fig. 2 are accounted for. Inspection of Fig. 3 shows that the received signal has about 1.3 s duration. The backpropagation is calculated by time reversing the received signal and retransmitting it from the receiver (now treated as a source), and from all the images of the receiver, using the same formalism as for the forward case. An example of the time-reversed transmissions to a matched position is shown in Fig. 4(a). Spatial resolution in source location depends on the reduction of the correlation maximum as the receiver is moved away from the matched position. Fig. 4(b) shows the effect of a 250-m range mismatch for the transmission shown in Fig. 4(a).

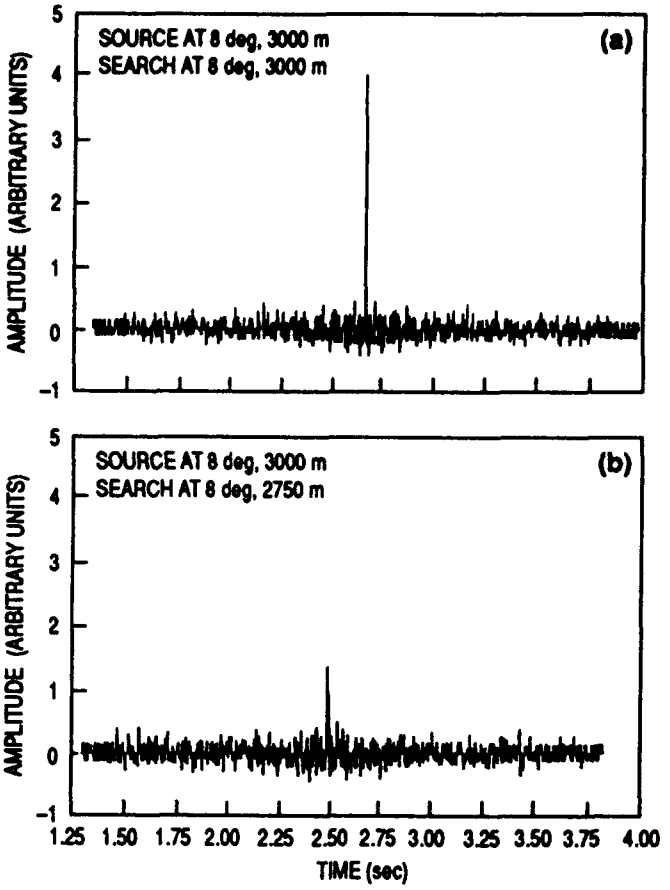

FIG. 4. Time reversed transmissions to matched and unmatched locations. In these examples the receiver location is 4 deg from surface and 1000 m range, $y=0$. The matched source location is: angle 8 deg from surface and 3000 m range, $y=0$. The unmatched location is angle 8 deg from surface and 2750 m range, $y=0$. The input signal was a 2-ms spike. (a) Matched location. (b) Unmatched location.

IV. MEASURES OF LOCALIZATION PERFORMANCE

Localization performance depends upon the number and positioning of receivers and the pulse duration (inversely proportional to the signal bandwidth). Performance is represented by the relative magnitudes of sidelobes as compared to the correlation maximum at the matched position (the main peak) and the spatial resolution of the peak.

A. Sidelobes

A maximum locator, defined as follows, gives a simple measure of relative amplitudes of the sidelobes

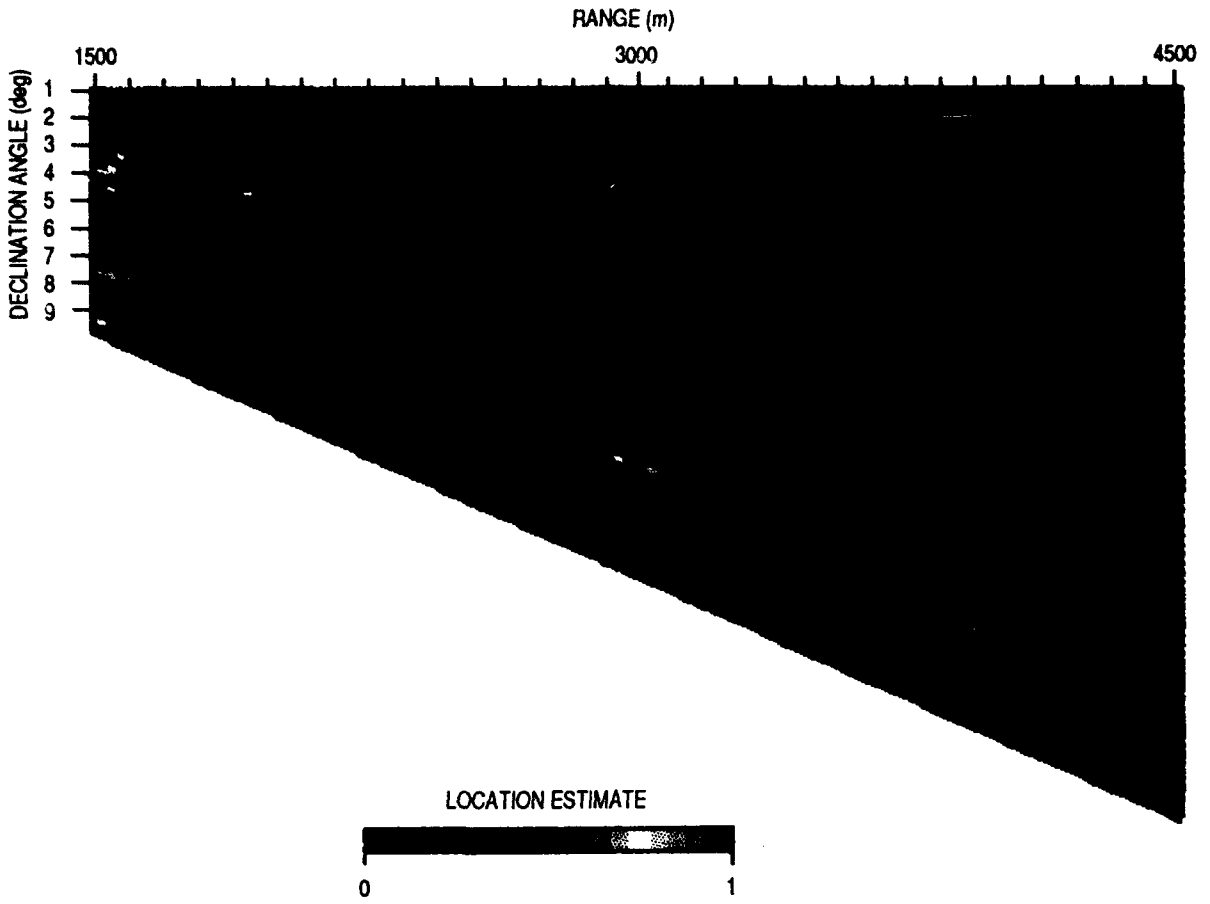

FIG. 5. Locator performance as a function of range and angle of declination. In this example the locator function L_P defined in Eq. (27) is plotted for a single receiver as a function of range from 1500 to 4500 m, and declination angle from 1 deg to 10 deg, for $y=0$ m. Source: angle 8 deg from surface and 3000 m range, $y=0$. Receiver: 4 deg from surface and 1000 m range, $y=0$. A 2-ms input spike was used.

$$L_P \equiv \frac{\max|p_M(t_l,Q)|}{\max|c_A(t_k,S)|}, \tag{27}$$

where t_l and t_k are the times of the respective maxima of the probe signal $|p_M(t_l,Q)|$ and the auto covariance $|c_A(t_k,S)|$.

A plot of the relative maxima of L_p as the probe receiver is moved from the matched position is a simple locator. An image of L_p for a single receiver is shown in Fig. 5. A 2-ms pulse was used for this example. The source was again placed at $r_S=3000$ m, $y_S=0$ m, $\Psi_S=8$ deg. The value of L_p is plotted as a function of range and declination angle. The plot shown in this figure clearly indicates a main peak at the correct range and angle. Spatial resolution is very good, even though only a single receiver has been used. Surrounding the main peak are several sidelobes. These are more pronounced on the side closer to the receiver. Toward the apex of the wedge they become quite large and the performance of the locator deteriorates. If P is the peak level in Fig. 5, while μ is the mean background level and σ the standard deviation of the background, a convenient way of quantifying the peak-to-background ratio is given by

$$\text{PBR}=10\ \log_{10}[(P-\mu)/\sigma]. \tag{28}$$

This can be viewed as a measure of detectability based upon the difference between the peak value and the mean background value, scaled in units of the standard deviation and expressed in dB.

B. Spatial resolution

How may the spatial resolution of the source in Fig. 5 be quantified? The radial width of the main signal peak is a localization parameter. Figure 6(a) shows a section through the peak, taken along a radial from the wedge apex, for the case represented in Fig. 5. We see that the maximum of L_p along the radial has a form very similar to a Gaussian, with ripple superimposed on it. In this study we have used a conjugate gradient technique to fit a Gaussian curve to this data, so that the signal peak radial width may be quantified by the Gaussian half-width ρ. By this means we can investigate how the addition and position of receivers, and changes of pulse duration, broadens or sharpens the peak. Another important parameter is the angular width of the main signal peak. Figure 6(b) shows a section through the signal peak, taken along an arc centered on the wedge apex, for the case represented in Fig. 5. We see that the source is very well resolved in angle, even with only one receiver. However, a number of sidelobes appear at discrete angles within the wedge. One of our aims here is to demonstrate how these "angle" sidelobes may be eliminated by adding more, angularly displaced, receivers.

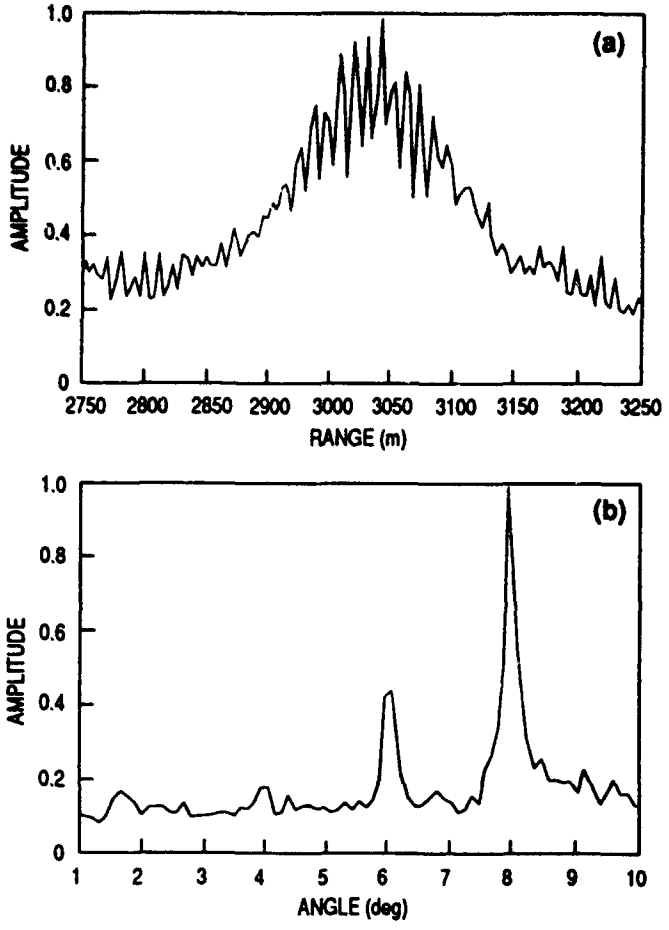

FIG. 6. Locator performance along radial and angular sections through the peak. Source: angle 8 deg from surface and 3000 m range, $y=0$. Receiver: 4 deg from surface and 1000 m range, $y=0$. A 2-ms input spike was used. (a) L_P is plotted as a function of range from 2750 to 3250 m, while the declination angle is 8 deg and $y=0$. (b) L_P is plotted as a function of declination angle from 1 to 10 deg, while the range is 3000 m and $y=0$.

V. SINGLE RECEIVERS AND PULSE DURATION

The main peak width and peak-to-background ratios were obtained and investigated as functions of (a) single receiver placement, (b) pulse duration, and (c) multiple receiver placement. For reference and comparison of performance of single and multiple receivers, in this section we describe the single receiver behavior.

In Fig. 7 we plot the variation of PBR and ρ for a 2-ms pulse case in which a source is placed at $r_S=3000$ m, $y_S=0$ m, $\Psi_S=8$ deg; and a single receiver is moved such that r_H varies from 500–1500 m, while y_H and Ψ_H are maintained at constant values of 0 m and 4 deg, respectively. The figure shows that both quantities improve significantly as the receiver is moved away from the wedge apex. The value of PBR increases steadily from about 9 dB when $r_H=500$ m to about 11.6 dB when $r_H=1250$ m, it then drops slightly to 11.5 dB at $r_H=1500$ m. The Gaussian half-width ρ falls from 240 m to about 45 m over the same interval. The reason for this improvement in performance is geometrical and easily understood if we look at Fig. 2, where the circle of source images (these will be images of the receiver in the reverse transmission procedure) is constructed. The radius of this

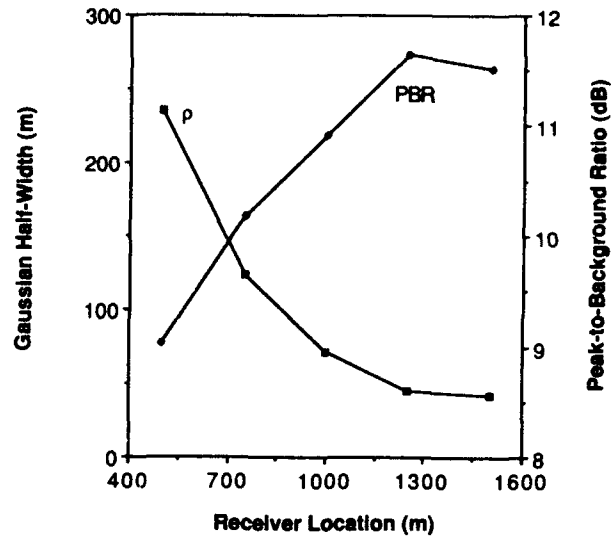

FIG. 7. Variation of peak-to-background ratio and half-width as a function of single receiver placement. PBR and ρ are plotted for a source at angle 8 deg from surface and 3000 m range, $y=0$. A 2-ms input spike was used. A single receiver was placed at angle 4 deg from surface and $y=0$. The receiver range varied from 500 to 1500 m.

circle increases as the source is moved further from the apex. This means that the maximum angle subtended by tangents from the circle to any point within the wedge also increases, so that the location of the point is more sharply and accurately fixed by triangulation. This decreases ρ directly, and also reduces the background variance and increases PBR by decreasing the opportunity for constructive addition of signals on different ray paths at locations other than the matched position.

The angular placement of the receiver can also have a very noticeable effect on the performance of the locator. In Fig. 8(a) we show the variation of L_p along an arc at $r_Q=1000$ m for a 2-ms pulse case in which the source is placed at $r_S=3000$ m, $y_S=0$ m, $\Psi_S=5.5$ deg; and the receiver is placed at $r_H=1000$ m, $y_H=0$ m, $\Psi_H=4$ deg. The main signal peak is seen at the correct source angle. However, there are also two prominent sidelobes positioned symmetrically on either side of the main peak. In Fig. 8(b) we show the equivalent curve when the receiver angle is $\Psi_H=8.5$ deg, while all the other parameters are unchanged. Again the main peak is clearly distinguished, but the sidelobes have disappeared. The sidelobe angles in Fig. 8(a) seem to be related to the relative angles of the source and receiver. If we write $\Psi_S=5.5$ deg and $\Psi_H=4$ deg, then it appears $\Psi_L=\Psi_S\pm2\{|\Psi_S-\Psi_H|\}$ (giving $\Psi_L=2.5$ and 8.5 deg in this case) for the sidelobes. When $\Psi_H=8.5$ deg the same formula gives $\Psi_L=-0.5$ and 11.5 deg, placing the sidelobes outside of the wedge so that they do not appear in Fig. 8(b).

The effect of bandwidth on the performance of the locator may be investigated indirectly by varying the time duration of the pulse signal. In the cases we have looked at so far we have used a 2-ms boxcar spike. This corresponds to a bandwidth ≅1 kHz. Now we will introduce a 1-ms spike (≅2-kHz bandwidth) and a 4-ms spike (≅500-Hz band-

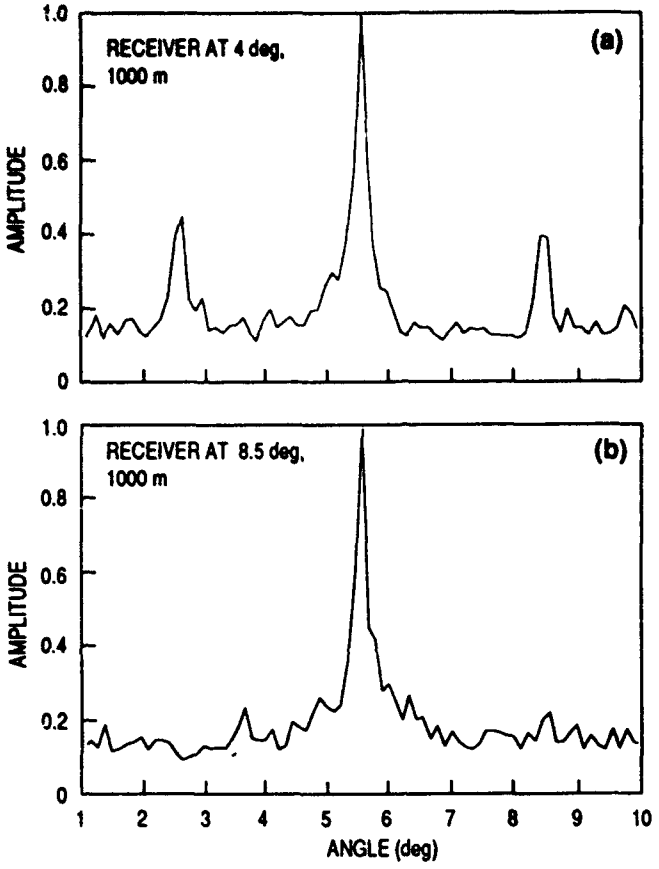

FIG. 8. Locator performance along angular sections for different receiver angles. The source is placed at angle 5.5 deg from surface and 3000 m range, $y=0$. A 2-ms input spike was used. L_P is plotted as a function of declination angle from 1 to 10 deg, while the range is 3000 m and $y=0$. (a) The receiver is placed 4 deg from surface and 1000 m range, $y=0$. (b) The receiver is placed 8.5 deg from surface and 1000 m range, $y=0$.

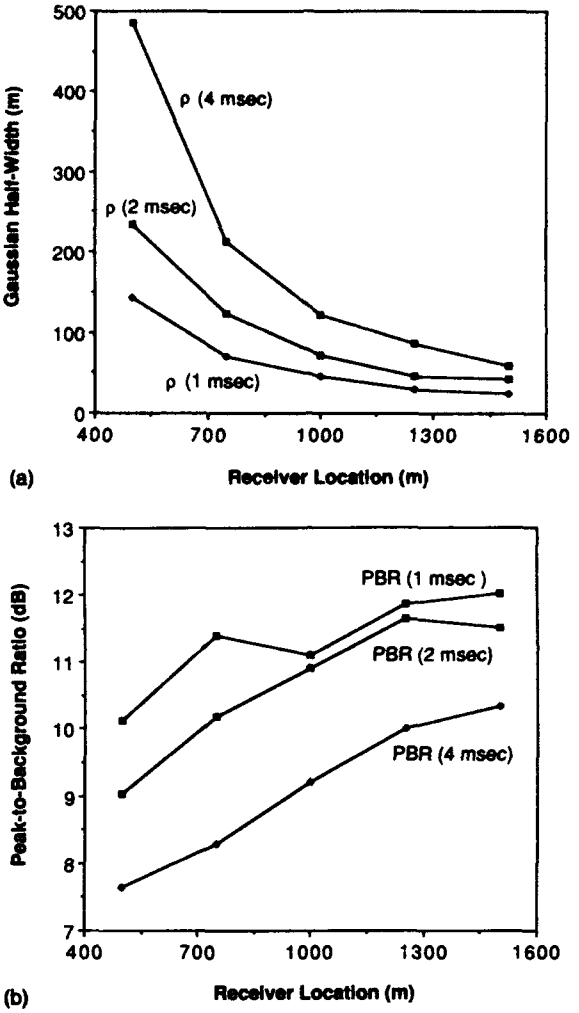

FIG. 9. Variation of peak-to-background ratio and half-width as a function of pulse duration. The source is placed at angle 8 deg from surface and 3000 m range, $y=0$. A single receiver was placed at angle 4 deg from surface and $y=0$. The receiver range varied from 500 to 1500 m. Three pulses were used: 1, 2, 4 ms. (a) Peak half-width ρ. (b) PBR.

width) also. In Fig. 9(a) we show the variation of ρ for the three pulse lengths, for a case in which a source is placed at $r_S=3000$ m, $y_S=0$ m, $\Psi_S=8$ deg; and a single receiver is moved such that r_H varies from 500–1500 m, while y_H and Ψ_H are maintained at constant values of 0 m and 4 deg, respectively (this is the same deployment used to produce Fig. 7). The figure clearly shows that the spatial resolution of the main peak, as measured by ρ, improves in direct proportion to the bandwidth and inversely to the duration of the pulse. The values of ρ shown in the figure do not indicate a strict linear relationship with the pulse duration. Figure 9(a) shows the narrowing behavior of the main peak for all three pulses as the receiver is moved further from the apex. In Fig. 9(b) we plot the PBR values for the three pulses as a function of receiver location. This quantity again improves in proportion to the bandwidth and clearly increases as the receiver is moved further from the apex, although some small fluctuations may be observed for the 1- and 2-ms pulses. Doubling the bandwidth seems to give between 0.25–1.5 dB of enhancement in PBR at each receiver location.

VI. MULTIPLE RECEIVER ARRAY

The rationale for putting multiple receiver arrays into the waveguide is that additional information is made available about the source by virtue of the multiplicity of ray paths to the many receiver/image locations. Arrays are expected to improve spatial resolution, reduce the background variance, and remove ambiguities by enhancing the effectiveness of source localization by triangulation, as we observed earlier while studying the placement of a single receiver. When adding further receivers, we can vary their placement position by changing r_H, y_H, or Ψ_H. These are orthogonal parameters within the wedge, and we will investigate their effect on the localization process independently of each other. Just as we did earlier in the study of single receiver position we will quantify this process by measuring the values of PBR and ρ, this time as functions of the array length.

In Fig. 10(a) we plot the variation of PBR and ρ for a 2-ms pulse where the source is placed at $r_S=3000$ m, $y_S=0$ m, $\Psi_S=8$ deg. Initially a single receiver is introduced at $r_H=1000$ m, $y_H=0$ m, $\Psi_H=4$ deg. Additional receivers are positioned so that they lie along a radial passing through the first receiver. The second is placed at $r_H=950$ m, $y_H=0$ m, $\Psi_H=4$ deg, forming a two element array of length 50 m. The third is placed at $r_H=1050$ m, $y_H=0$ m, $\Psi_H=4$ deg, making

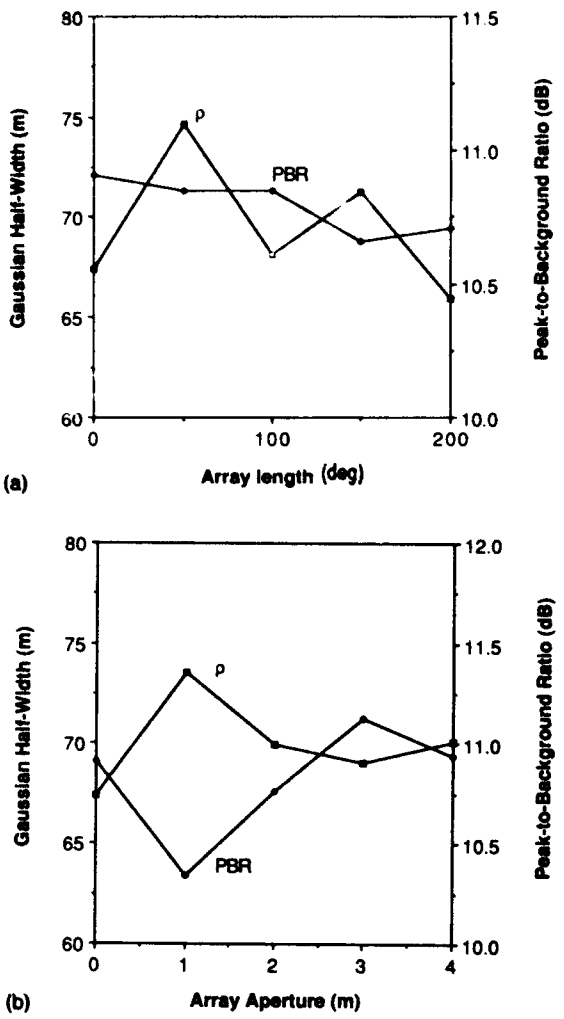

FIG. 10. Variation of peak-to-background ratio and half-width as a function of array length. The source is placed at angle 8 deg from surface and 3000 m range, $y=0$. A 2-ms input spike was used. The first receiver is placed at angle 4 deg from surface, range 1000 m and $y=0$. (a) PBR and ρ are plotted as additional receivers are introduced at 50 m range intervals, with the same angle and y as the first receiver. (b) PBR and ρ are plotted as additional receivers are introduced at 1-deg angular intervals, with the same range and y as the first receiver.

a 100-m array. A fourth and fifth receiver are introduced at $r_H=900$ m and $r_H=1100$ m, increasing the array length to 150 and 200 m, respectively. We see that with only one receiver the Gaussian half-width ρ is about 67.5 m. When the receiver at 950 m is added, ρ increases to slightly less than 75 m. The reason for this increase is clear from Fig. 7. Receivers closer to the wedge apex resolve the source less well, so that backpropagation from the second receiver produces a broader signal peak than from the first. Locating on the aggregate signal from the two receivers (i.e. processing them as a two element array) gives a poorer result than is achieved with the first receiver alone. The opposite effect is observed when a third receiver is added at 1050 m, which decreases ρ to 68 m. The pattern is repeated when the fourth and the fifth receivers are introduced: ρ increases to 71 m and then decreases again to 66 m. It appears that, contrary to expectations, the aggregation of signals from multiple receivers does not lead to a monotonic improvement in spatial resolution of the source, unless the secondary receivers are further from

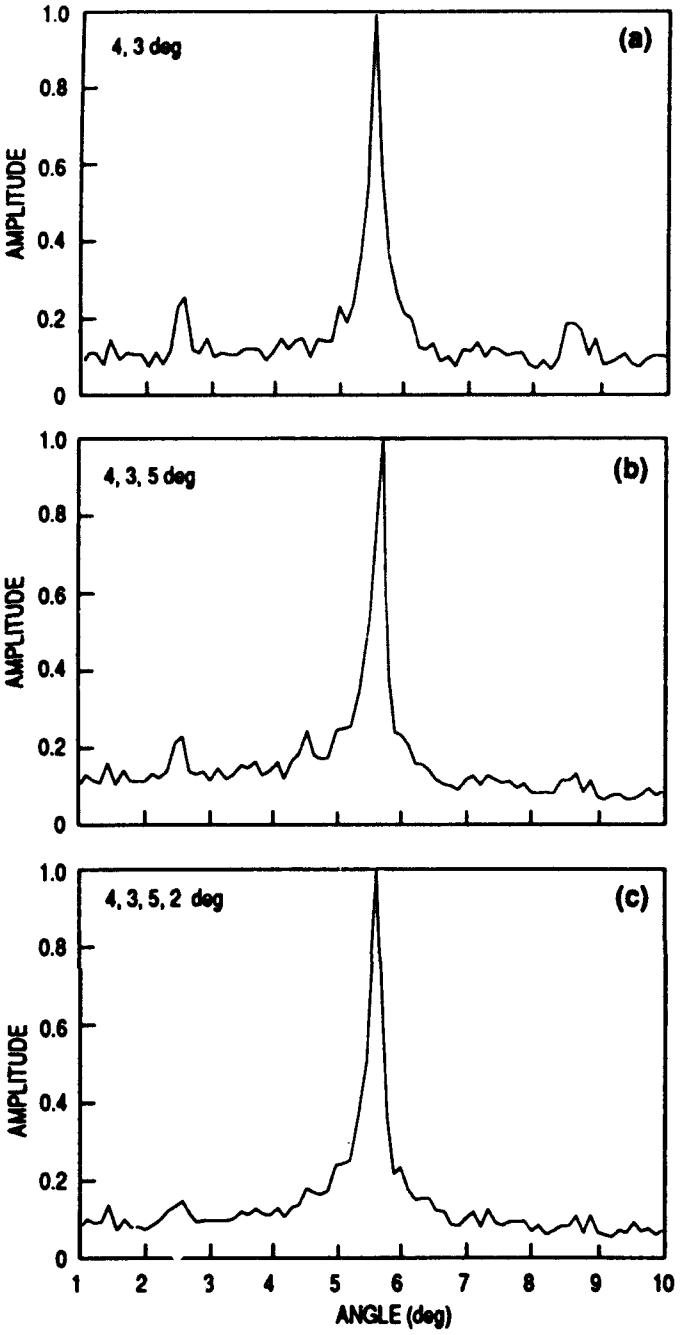

FIG. 11. Suppression of "angle" sidelobes by addition of receivers. The source is placed at angle 5.5 deg from surface and 3000 m range, $y=0$. A 2-ms input spike was used. All receivers are placed at range 1000 m and $y=0$. L_P is plotted as a function of declination angle from 1 to 10 deg, while the range is 3000 m and $y=0$. (a) Two receivers: 3 and 4 deg. (b) Three receivers: 3, 4, and 5 deg. (c) Four receivers: 2, 3, 4, and 5 deg.

the wedge apex than the primary receiver. This is a surprising result, but more significant is the fact that the fluctuations in ρ are so small. The spread in values is only 9 m; and the 200-m long array has the total effect of reducing ρ by only 1.5 m from the value achieved using a single receiver. This is in complete contrast to the improvements that can be obtained by judicious positioning of a single receiver, as we observed earlier. The variations in PBR shown in the same figure mirror and complement the ρ results. This falls from an initial value of 10.9 dB for the single (1000 m) receiver to

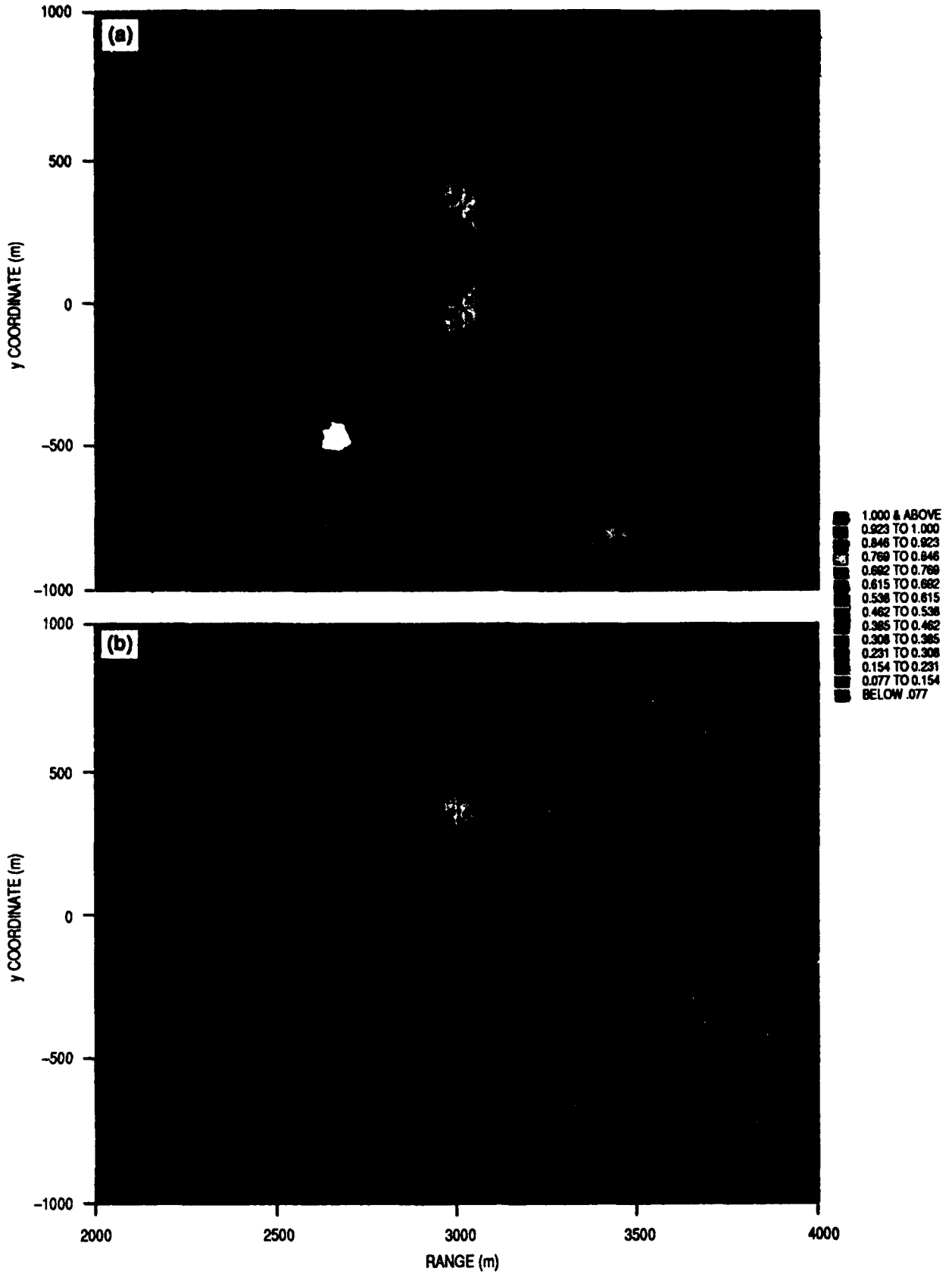

FIG. 12. Locator performance as a function of range and y for multiple lateral receivers. The locator function L_P is plotted as a function of range from 2000 to 4000 m, and y from -1000 to 1000 m, with a declination angle of 4 deg. Source: angle 8 deg from surface and 3000 m range, $y=350$ m. A 2-ms input spike was used. All receivers are placed 4 deg from the surface and at range 1000 m. (a) One receiver: $y=150$ m. (b) Two receivers: $y=150$ and 200 m.

10.8 dB when the second (950 m) receiver is added. It maintains this value with the third (1050 m) receiver and then falls again to 10.6 dB with the fourth (900 m). Finally it rises slightly to 10.7 dB with the introduction of the fifth (1100 m) receiver. All of the variations are very small, with a spread of only 0.3 dB. It seems that the addition of more receivers, and aggregating signals over a wide range aperture, does not smooth-out sidelobes in the waveguide or decrease the background variance. Again, it would be better to use a single receiver and move it further from the wedge apex. We also looked at the change in angular resolution of the source with the use of multiple, radially displaced, receivers. No significant effect was observed.

In Fig. 10(b) we again plot the variation of PBR and ρ for a 2-ms pulse with the source placed at $r_S=3000$ m, $y_S=0$ m, $\Psi_S=8$ deg. As before, the first receiver is placed at $r_H=1000$ m, $y_H=0$ m, $\Psi_H=4$ deg. This time, however, additional receivers are positioned so that they lie along an arc passing through the first receiver. The second is placed at $r_H=1000$ m, $y_H=0$ m, $\Psi_H=3$ deg, forming a two element array of angular aperture 1 deg. The third is placed at $r_H=1000$ m, $y_H=0$ m, $\Psi_H=5$ deg, making a 2-deg array. A fourth and fifth receiver are introduced at $\Psi_H=2$ deg and $\Psi_H=6$ deg, increasing the array aperture to 3 and 4 deg, respectively. With only one receiver the Gaussian half-width ρ is about 67.5 m. When the receiver at $\Psi_H=3$ deg is added, ρ increases to slightly less than 74 m. It then decreases again as the $\Psi_H=5$ deg is added and levels off at around 70 m. As in Fig. 10(a), the PBR curve appears to mirror the ρ curve. It falls from an initial value of 10.9 dB to about 10.3 dB for two receivers. It then increases again to a peak of 11.1 dB, and falls finally to 10.9 dB for the 4-deg aperture. These changes in ρ and PBR are probably due to the introduction of receivers which, depending upon the contingencies of their own location, give better or poorer individual performance. Again they are quite minor, and it seems that the addition of more receivers, and aggregating signals over the angular aperture, does not smooth-out sidelobes in the waveguide or decrease the background variance.

Although the introduction of angularly displaced receivers does not change the radial width ρ of the peak, it has a notable effect on the angular resolution performance. In Fig. 11(a) we show the variation of L_p along an arc at $r_Q=1000$ m for a 2-ms pulse with the source placed at $r_S=3000$ m, $y_S=0$ m, $\Psi_S=5.5$ deg. Two receivers are placed: one at $r_H=1000$ m, $y_H=0$ m, $\Psi_H=4$ deg; and a second with $\Psi_H=3$ deg. This figure should be compared with Fig. 8(a), which was produced using the same deployment but with only the $\Psi_H=4$ deg receiver. We see that the angular resolution of the main peak is about the same in the two cases, but the amplitude of the sidelobes on either side of the peak is much reduced due to the presence of the second receiver. In Figs. 11(b) and 11(c) we show the response when receivers are added at $\Psi_H=5$ deg and $\Psi_H=2$ deg, respectively. In Fig. 11(b) the sidelobes may still be discerned, but in Fig. 11(c) they have essentially disappeared.

Let us now look at the effect of positioning multiple receivers at laterally displaced locations (i.e. with variable y_H values). In Fig. 12(a) we plot L_p as a function of r_Q and y_Q (with Ψ_Q held constant at 4 deg) for a 2-ms pulse case with the source at $r_S=3000$ m, $y_S=350$ m, $\Psi_S=8$ deg and a single receiver at $r_H=1000$ m, $y_H=150$ m, $\Psi_H=4$ deg. We see that the one receiver is able to locate the source quite sharply, but that it gives rise to mirror-image ambiguities on either side of a radial passing through the receiver location at $y_Q=150$ m, so that a second signal peak appears at $y_Q=-50$ m. The introduction of a second receiver at $y_H=200$ m immediately removes the ambiguity and improves the spatial resolution, as we see in Fig. 12(b). The addition of more receivers also reduces the background variance. Figure 13 shows that PBR increases with the number of receivers, indicating enhanced smoothing of sidelobes, although the rate of improvement seems to slowly dec.ease. We also studied the effect of adding laterally displaced receivers on the radial width (ρ) and the angular resolution of the source peak. No significant effect was observed.

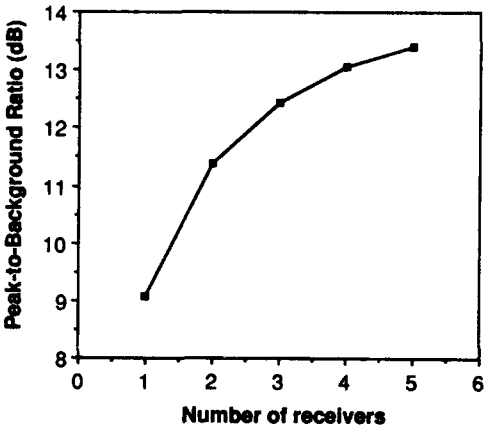

FIG. 13. Variation of peak-to-background ratio with number of lateral receivers. Source: angle 8 deg from surface and 3000 m range, $y=350$ m. A 2-ms input spike was used. All receivers are placed 4 deg from the surface and at range 1000 m. PBR is plotted as receivers are introduced at $y=150$, 200, 100, 250, and 50 m.

VII. CONCLUSIONS

Adding more receivers, in either a radial or angular configuration, has an insignificant effect in reducing the peak width or improving the peak-to-background ratio. The addition of more receivers in a lateral configuration leads to sharp and unambiguous azimuthal localization of the source and improves the peak-to-background ratio. The range-dependent characteristics of a wedge waveguide facilitate source localization. "Range" sidelobes, which are a typical complication in a range-independent environment, are eliminated even when only a single hydrophone is used. "Angle" sidelobes may be effectively eliminated by introducing additional receivers angularly spaced in the waveguide, at a constant range from the apex. Both the peak width and the peak-to-background ratio improve in proportion to the inverse bandwidth of the input signal. If one has the choice to make location experiments, wedges are much better than nice uniform waveguides. It may be speculation, but we think that source localization improves with the complexity of the range dependency of the environment. Of course, this requires solution of the acoustic transmission problem for a large frequency bandwidth.

ACKNOWLEDGMENTS

This work was sponsored by the Naval Research Laboratory 6.1 Program (CF), Element number 61153N (Dr. E. K. Franchi); and by the Office of Naval Research (CSC), under Contract N00014-89-J-1515 (Dr. Marshall Orr); and by the Office of Naval Technology (CSC), Program Element 0602435N (Roger Meredith). NRL Contribution Number NRL/JA/7174-92-0002. Geophysical and Polar Research Center, University of Wisconsin—Madison Contribution Number 555.

APPENDIX: GEOMETRICAL CONSTRUCTION OF REFLECTED RAY PATHS

The total pressure field at the receiver location due to the direct arrival from the source and the reflected arrivals from the images is given by Eq. (9), which contains two summations. Examination of this equation shows that each separate term within the summations uniquely represents a single transmission path from either the source or one of its images to the receiver; and that each term also incorporates (via $\mathscr{R}_{1,0}$ and $\mathscr{R}_{1,2}$) the boundary reflections experienced by the transmission as it traverses the path which it represents. We also note that the source and images are represented by terms in either the $(-+)$ summation or the $(--)$ summation, indicating that the transmissions fall into two distinct families.

A simple and beautiful geometrical construction may be performed which clearly illustrates the application of Eq. (9) and facilitates the calculation of the ray paths, especially in cases where the reflection coefficients $\mathscr{R}_{1,0}$ and $\mathscr{R}_{1,2}$ are dependent upon the angle of incidence at the boundaries. It also greatly simplifies transmission calculations in a finite wedge, as we shall also show. To demonstrate this construction we consider the case of a 35-deg wedge, with a source and receiver positioned so that the source is closer to the apex. Figure A1 shows the wedge and the source and receiver locations, and uses several images of the source to construct one of the ten or so available ray paths from the source to the receiver. We see in the figure the source (labeled A) and all the images of the source symmetrically positioned around the apex as determined by the image reconstruction theory described in Sec. I. The particular ray depicted originates at A and is first reflected by the bottom at B, making an angle α_B with the bottom surface. (For the purposes of this discussion it is convenient to use the complement to the angle of incidence rather than the angle of incidence itself.) When reflected the ray is modified by the reflection coefficient which, if it is angle dependent, may be written in this case as $\mathscr{R}_{1,2}(\alpha_B)$. The ray then travels to the water surface which it meets at C. It makes an angle α_C with this boundary and reflects from it, modifying the ray by $\mathscr{R}_{1,0}(\alpha_C)$. The ray then reflects a second time from the bottom surface at D: the angle is α_D and the reflection coefficient is $\mathscr{R}_{1,2}(\alpha_D)$. Finally the ray reaches the receiver at F. The partial pressure field at F due to this single ray may be determined by isolating the appropriate term from the summations in Eq. (9). In this case it may be written

$$p_{A\to F}(t)=[P_0\ R_0]\mathscr{R}_{1,2}(\alpha_B)\mathscr{R}_{1,0}(\alpha_C)\mathscr{R}_{1,2}(\alpha_D)\times\frac{\delta[t-R_{-1}(--)/c]}{R_{-1}(--)}. \tag{A1}$$

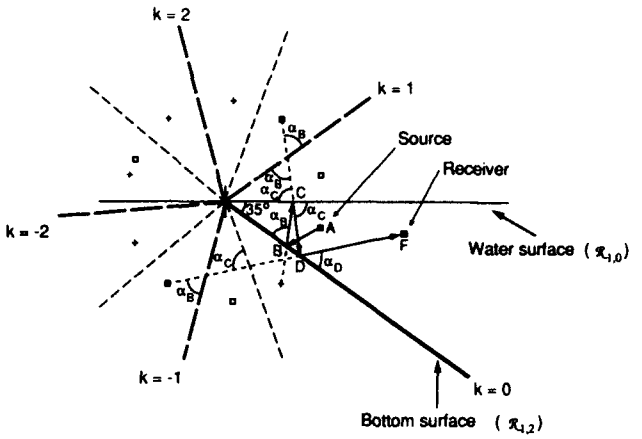

FIG. A1. A sample ray path construction. Several of the source images are used to construct one of the possible ray paths between the acoustic source at A and the receiver at F. A similar construction may be performed for each of the images shown. The images of the surfaces of the wedge reflected in each other are also shown. The "kaleidoscopic" relationship between the source and surface images is apparent. Geometrical reasoning may be used to demonstrate the equivalence of all the angles labeled α_B, and also those labeled α_C and α_D.

We see that $k=-1$ for this transmission and that it lies in the $(--)$ family. The total length of the ray path is $R_{-1}(--)$.

In addition to the images of the source reflected in the surfaces of the wedge, Fig. A1 also shows the images of the wedge surfaces themselves reflected in each other. (Careful examination of the figure shows that the surfaces are reflected and rereflected in each other to form a kaleidoscope of images around the apex.) We may describe the pattern that results from this as follows: Starting at the water surface and proceeding in a counterclockwise direction around the apex we encounter, after turning 35 deg, the first $(k=1)$ image of the bottom surface reflected in the water surface (this is drawn as a thick line with long dashes). Turning another 35 deg we find the first image of the water surface (drawn as a thinner line with shorter dashes). Another 35 deg brings the second $(k=2)$ image of the bottom surface, and a further 35 deg leads to the second image of the water surface. If we then go over to the original bottom surface, and start turning successive increments of 35 deg in a clockwise direction, we can explain the remaining surface images in a similar manner. We should note here the angular relationship of these wedge surface images to each other and to the images of the source. Bearing in mind the mathematical constructions of both types it follows, after some consideration of the reflection symmetry in the problem, that the images of the surfaces perfectly bisect the angular locations of the pairs of source images between which they pass. (It again helps to think in terms of a kaleidoscope to see this.) Using basic geometrical arguments the reader may easily satisfy himself that this is true and also prove the equivalence of the sets of angles labeled α_B and α_C in Fig. A1.

In Fig. A2 we consider the same ray transmission depicted in Fig. A1, but this time it is represented by a straight line drawn directly between the originative source image (labeled A′) and the receiver at F. This is an equivalent construction of the ray path. We can show this and also demon-

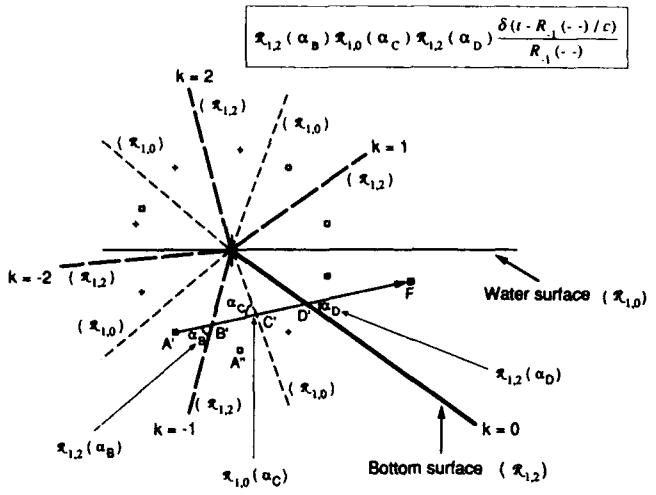

FIG. A2. Alternative ray path construction. An equivalent description of the ray path in Fig. A1 is shown. Reflection at the surfaces of the wedge is now represented by transmission through the images of those surfaces with the same angles of incidence (compare angles α_B, α_C, and α_D in this figure and Fig. A1). The total path length and the lengths of the various sections of the paths are the same in both figures. The ray path expansion [Eq. (A1)] contains the product of three reflection coefficients. The image originating the ray is in the $(--)$ family.

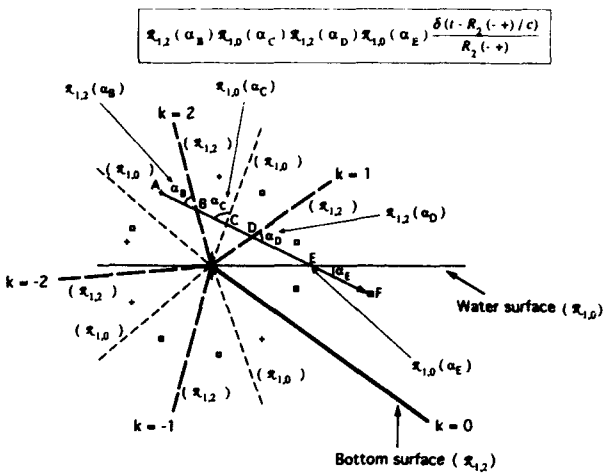

FIG. A3. A higher-order ray path. The ray shown here involves four reflections at the wedge surfaces, and this is represented by transmission through the surface images as indicated. The ray path expansion [Eq. (A2)] contains the product of four reflection coefficients. The image originating the ray is in the $(-+)$ family.

strate that all of the events occurring within the transmission path from A to F shown in Fig. A1 may be correctly (and more easily) described by considering the transmission path from A′ to F in Fig. A2. First of all we will consider the overall length of the two paths. By comparing Figs. A1 and A2, and using symmetry and geometry, we can see that the line segment AB is the same length as A′B′. Similarly BC is the same length as B′C′, and CD is the same length as C′D′. The segments DF and D′F are identical. Adding the segments together for the two figures shows that the two paths are the same length and equal to $R_{-1}(--)$. Now let us follow the transmission from A′ to F in Fig. A2. The ray starts at A′ and travels a distance A′B′ (same as AB) to the $k=-1$ image of the bottom surface, which it meets with angle α_B. Since this surface image is a reflection of the $\mathscr{R}_{1,2}$ boundary, passage of the ray through it indicates a modification of the ray by the reflection coefficient $\mathscr{R}_{1,2}(\alpha_B)$. The ray then travels B′C′ (same as BC) to the next image of the water surface, which it meets with angle α_C. This image is a reflection of the $\mathscr{R}_{1,0}$ boundary, and transmission through it therefore indicates a modification of the ray by $\mathscr{R}_{1,0}(\alpha_C)$. The ray then travels C′D′ (same as CD) to the bottom surface, which it meets with angle α_D. Passage through this indicates a modification of the ray by $\mathscr{R}_{1,2}(\alpha_D)$. The ray then travels D′F to the receiver. If we make a piece by piece comparison of the path just described with the path AF in Fig. A1 we see that, at every stage, they are identical and are both described by Eq. (A1). The partial pressure at the receiver F due to the ray A′F is given by $p_{A'\to F}(t)=p_{A\to F}(t)$. The main difference in the usage of Eq. (A1), when working in the image space shown in Fig. A2, is that the changes to the ray indicated by the reflection coefficients $\mathscr{R}_{1,0}$, $\mathscr{R}_{1,2}$ etc. are applied as the ray passes *through* the surfaces, rather than being reflected by them.

Using Fig. A2 it is possible to provide further illumination of Eq. (A1) and of all the other terms in Eq. (10). We recall that the ray path AF in Fig. A1 (and hence A′F in Fig. A2) lies in the $(--)$ family of terms with $k=-1$. Looking at Fig. A2 we note that the source image A′ is positioned immediately beside the $k=-1$ reflection of the bottom surface. It turns out that the ray path to the receiver from the image A″, on the opposite side of the $k=-1$ bottom surface reflection from A′, is also given by a $k=-1$ term in Eq. (10), but lies in the $(-+)$ family. This is true for all the pairs of images lying on either side of the various reflections of the bottom surface in the image space. The ray paths from them to the receiver will be labeled by the k value of the bottom reflection to which they are adjacent, and they will alternately fall into the $(--)$ and $(-+)$ families. We can now see that, rather than thinking in terms of the ray paths, we can identify the images *themselves* according to their k value and family. In Fig. A3 we show a ray path between another of the source images and the receiver. This image lies adjacent to the $k=2$ reflection of the bottom surface and is identified as a $k=2$ image in the $(-+)$ family. A straight line drawn between it and the receiver indicates that the ray undergoes four boundary interactions this time (note that in this figure we have used a fresh lettering scheme for the source and receiver and points of interaction with the boundaries). The partial pressure field may again be determined by isolating the appropriate term from the summations in Eq. (10). In this case it is

$$p_{A\to F}(t)=[P_0\,R_0]\mathscr{R}_{1,2}(\alpha_B)\mathscr{R}_{1,0}(\alpha_C)\mathscr{R}_{1,2}(\alpha_D)\mathscr{R}_{1,0}(\alpha_E)\times\frac{\delta[t-R_2(-+)/c]}{R_2(-+)}. \tag{A2}$$

From the foregoing discussion, we can now see how algorithms may be developed to perform ray transmission computations for the general wedge problem, in which the wedge angle as well as the source and receiver locations and the wedge surface reflectivities are variable parameters. The ray paths may be calculated geometrically. First, the wedge

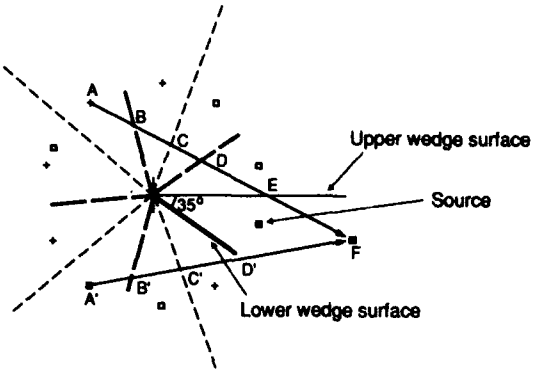

FIG. A4. Allowed and disallowed ray paths in a finite wedge. Images of the source and surfaces are shown in a wedge with finite faces of unequal length. The ray path AF will successfully reflect between the two surfaces of the wedge and connect the source and receiver. The other path A′F misses one surface at D′ and therefore does not exist.

would be drawn and all the reflections of the bottom and water surfaces. Second, the source would be positioned and all of its images together with the receiver. Third, rays would be drawn between the images and the receiver, and the path lengths $R_k(--)$ and $R_k(-+)$ calculated for all k. Fourth, the angles at which the rays cross the surface reflections (α_B, α_C,..., etc) and the associated reflectivities [$\mathscr{R}_{1,2}(\alpha_B)$, $\mathscr{R}_{1,0}(\alpha_C)$,... etc] would be determined (we can represent the rays and surfaces algebraically, so finding their points and angles of intersection is straightforward). Finally, the pressure field contributions from all of the images may be enumerated individually [Eqs. (A1) and (A2) give two examples] and then added together.

A particularly interesting consequence of this procedure applies to the case of finite wedges, i.e., when the faces are of finite and generally unequal length. In Fig. A4 we show a 35-deg wedge for which the lower surface is much shorter than the upper surface. An important question to ask here is, for an arbitrary placement of source and receiver, which ray paths will be able to perform multiple reflections from both surfaces of the wedge and successfully connect the source and receiver? This question is quite simply answered if we construct the images of the source around the apex, as before, and also the images of the surfaces. We note that the surface images are now of different lengths; longer or shorter, depending upon whether they are reflections of the upper or lower surface, respectively. We then connect the source images to the receiver by straight lines. If a given line passes through all the surfaces, then the ray path it represents is allowed. If the line misses even one surface, the ray is not allowed. In the figure the ray AF is allowed. The other ray A′F is not allowed (it misses at D′). Since the reflection coefficient $\mathscr{R}_{1,2}$ or $\mathscr{R}_{1,0}$ is obviously zero at any surface which the ray misses, then any term in Eq. (10) in which that coefficient appears, e.g., Eq. (A1), will be zero. Its contribution to the total pressure field at the receiver will also be zero, i.e., the ray does not exist.

[1] H. P. Bucker, "Use of calculated sound fields and matched-field detection to locate sound sources in shallow water," J. Acoust. Soc. Am. **59**, 368–373 (1976).

[2] R. M. Heitmeyer, W. B. Moseley, and R. G. Fizell, "Full-field ambiguity processing in a complex shallow-water environment," in *High-Resolution Spatial Processing in Underwater Acoustics*, edited by R. A. Wagstaff and A. B. Baggeroer (US Government Printing Office), NORDA publication 1985-570-276, (1985), pp. 171–188.

[3] C. Feuillade, W. A. Kinney, and D. R. DelBalzo, "Shallow-water matched-field localization off Panama City, Florida," J. Acoust. Soc. Am. **88**, 423–433 (1990).

[4] G. B. Smith, C. Feuillade, and D. R. DelBalzo, "Matched-field processing enhancement in a shallow-water environment by incoherent broadband averaging," J. Acoust. Soc. Am. **91**, 1447–1455 (1992).

[5] C. S. Clay, "Optimum time domain signal transmission and source location in a waveguide," J. Acoust. Soc. Am. **81**, 660–664 (1987).

[6] S. Li and C. S. Clay, "Optimum time domain signal transmission and source location in a waveguide: Experiments in an ideal wedge waveguide," J. Acoust. Soc. Am. **82**, 1409–1417 (1987).

[7] C. S. Clay and S. Li, "Time domain signal transmission and source location in a waveguide: Matched filter and deconvolution experiments," J. Acoust. Soc. Am. **83**, 1377–1383 (1988).

[8] W. S. Hodgkiss and R. K. Brienzo, "Broadband source detection and range/depth localization via full-wave (matched field) processing," Proc. ICASSP-90, 2743–2747 (1990).

[9] L. N. Frazer and P. I. Pecholcs, "Single-hydrophone localization," J. Acoust. Soc. Am. **88**, 995–1002 (1990).

[10] C. Feuillade and C. S. Clay, "Source imaging and sidelobe suppression using time-domain techniques in a shallow-water waveguide," J. Acoust. Soc. Am. **92**, 2165–2172 (1992).

[11] I-Tai Lu, H.-Y. Chen, and P. Voltz, "A matched-mode processing technique for localizing a transient source in the time domain," J. Acoust. Soc. Am. **93**, 1365–1373 (1993).

[12] I. Tolstoy and C. S. Clay, *Ocean Acoustics: Theory and Experiment in Underwater Sound* (American Institute of Physics, New York, 1987), 2nd ed.

[13] C. S. Clay, *Elementary Exploration Seismology* (Prentice-Hall, Englewood Cliffs, NJ, 1990), Chaps. 15 and 16.

[14] D. R. Jackson and D. R. Dowling, "Phase conjugation in underwater acoustics," J. Acoust. Soc. Am. **89**, 171–181 (1991).

[15] J. Claerbout, *Imaging the Earth's Interior* (Blackwell, Oxford, 1985).

[16] M. A. Biot and I. Tolstoy, "Formulation of wave propagation in infinite media by normal coordinates with an application to diffraction," J. Acoust. Soc. Am. **29**, 381–391 (1957).

[17] D. Chu, "Impulse response of density contrast wedge using normal coordinates," J. Acoust. Soc. Am. **86**, 1883–1896 (1989).

[18] M. J. Buckingham, "Theory of three-dimensional acoustic propagation in a wedgelike ocean with a penetrable bottom," J. Acoust. Soc. Am. **82**, 198–210 (1987).

[19] L. M. Brekhovskikh, *Waves in Layered Media* (Academic, Orlando, 1980), 2nd ed., pp. 104–107.

[20] C. T. Tindle and G. E. J. Bold, "Improved ray calculations in shallow water," J. Acoust. Soc. Am. **70**, 813–819 (1981).

[21] C. T. Tindle and G. B. Deane, "Sound propagation over sloping bottom using rays with beam displacement," J. Acoust. Soc. Am. **78**, 1366–1374 (1985).

[22] N. G. Plumpton and C. T. Tindle, "Saddle point analysis of the reflected acoustic field," J. Acoust. Soc. Am. **85**, 1115–1123 (1989).

[23] G. B. Deane and M. J. Buckingham, "An analysis of the three-dimensional sound field in a penetrable wedge with a stratified fluid or elastic basement," J. Acoust. Soc. Am. **93**, 1319–1328 (1993).

[24] I. Tolstoy, *Wave Propagation* (McGraw-Hill, New York, 1973).

[25] W. A. Kinney, C. S. Clay, and G. A. Sandness, "Scattering from a corrugated surface: Helmholtz–Kirchhoff theory and the facet-ensemble method," J. Acoust. Soc. Am. **73**, 183–194 (1983).

[26] D. Chu, "Exact solution for a density contrast shallow-water wedge using normal coordinates," J. Acoust. Soc. Am. **87**, 2442–2450 (1990). This paper contains an extended list of references on the wedge problem.

[27] H. Medwin, "Shadowing by finite noise barriers," J. Acoust. Soc. Am. **69**, 1060–1064 (1981).

[28] S. Li and C. S. Clay, "Sound transmission experiments from an impulsive source near rigid wedges," J. Acoust. Soc. Am. **84**, 2135–2143 (1988).

[29] A. Parvulescu and C. S. Clay, "Reproducibility of signal transmissions in the ocean," Radio Eng. Electron. **29**, 223–228 (1965), Sec. 7.7, Tolstoy and Clay, Ref. 12.